Journal of Alloys and Compounds 509 (2011) 10025–10031

Contents lists available at ScienceDirect

Journal of Alloys and Compounds

journal homepage: www.elsevier.com/locate/jallcom

Effects of mineralizing agent on the morphologies and photoluminescence properties of Eu^{3+}-doped ZnO nanomaterials

Jinghai Yang[a,b,*], Xue Li[a,b,c], Jihui Lang[a,b], Lili Yang[a,b], Ming Gao[a,b], Xiaoyan Liu[a,b], Maobin Wei[a,b], Yang Liu[a,b], Rui Wang[a,b]

[a] Institute of Condensed State Physics, Jilin Normal University, Siping 136000, PR China
[b] Key Laboratory of Functional Materials Physics and Chemistry (Jilin Normal University), Ministry of Education, Siping 136000, PR China
[c] College of Materials Science and Engineering, Beijing University of Chemical Technology, Beijing 100029, PR China

ARTICLE INFO

Article history:
Received 25 November 2010
Received in revised form 3 August 2011
Accepted 4 August 2011
Available online 11 August 2011

Keywords:
Eu-doped ZnO nanomaterials
Mineralizing agent
Hydrothermal method
Photoluminescence properties

ABSTRACT

Eu-doped ZnO nanomaterials with different morphologies were successfully synthesized with various mineralizing agents by the mild hydrothermal method. The mineralizing agent was found to have strong effect on the crystal structures, morphologies and photoluminescence properties of the samples. Transmission electron microscopy and scanning electron microscopy images showed the Eu-doped ZnO nanorods, nanoneedles and cactus-like microspheres based on nanosheets can be fabricated by choosing NaOH, $C_6H_{12}N_4$ and $(NH_2)_2CO$ as the mineralizing agents, respectively. The results from X-ray diffraction and X-ray photoelectron spectroscopy indicated europium ions with trivalent valence were successfully doped into the crystal lattice of ZnO matrix. In the PL spectra from the Eu-doped ZnO nanomaterials synthesized with mineralizing agents of NaOH or $(NH_2)_2CO$, three separated red emissions can be obviously observed, which can be attributed to the 4f–4f intrashell transitions of $^5D_0 \rightarrow {}^7F_0$, $^5D_0 \rightarrow {}^7F_1$ and $^5D_0 \rightarrow {}^7F_2$ of Eu^{3+} ions, respectively. The intensity of red emission was found to be related with the concentration of intrinsic defects, especially O-vacancies, which could assist the energy transfer from the ZnO host to the Eu^{3+} ions.

1. Introduction

ZnO is a major potential candidate for optoelectronic applications due to its wide bandgap energy of 3.37 eV at room temperature and large exciton binding energy (60 meV) [1–3]. The ability of emitting visible light turns it to be a promising material for the flat panel displays, florescence labels for biological imaging, and so on. As well as we known, the possibility of practical application of any semiconductor lies on the effective manipulation of its physical properties. No doubt, doping selective elements into ZnO matrix offers an effective method to realize it. To date, ZnO has been widely used as a host matrix for the visible and infrared emission of various rare-earth ions [4,5]. For instance, trivalent europium ion as one of famous rare earth (RE) ions can be introduced into ZnO nanomaterials to produce red emission [6–8]. In addition, the synthesis of nanomaterials with special size and morphology has attracted more attention due to their potential applications in various fields such as photoelectronic devices, biological diagnostic probes, catalyst, etc. [9–11]. Up to now, various techniques have been developed for controlling shape, size and structures of such nanomaterials [12–19]. Moreover, the spontaneous emission probability of rare-earth doping nanoparticles can be significantly modified by changing the particle size, shape and surrounding medium [20–25]. However, the investigation about the Eu-doped ZnO nanomaterials with different morphology, in particular, the effects of various mineralizing agents on their morphologies and photoluminescence properties are limited [26,27]. Therefore, developing a suitable method to synthesize the Eu^{3+}-doped ZnO nanostructures with various morphologies for tuning their optical properties is still a challenge.

In this paper, Eu-doped ZnO nanomaterials with different morphologies are synthesized by the mild hydrothermal method with adding various mineralizing agents, and their morphologies, growth mechanism and photoluminescence properties are discussed in detail.

2. Experimental

Analytical pure $Zn(NO_3)_2{\cdot}6H_2O$, Eu_2O_3, NaOH, $C_6H_{12}N_4$ (HMT) and $(NH_2)_2CO$ were used as initial materials. Firstly, appropriated amounts of europium oxide (Eu_2O_3) were dissolved in concentrated nitric acid, and then heated at 120 °C for 1 h. A certain amounts of distilled water was added to the above mixture to form the 0.1 mM of $Eu(NO_3)_3$ solution. Secondly, $Zn(NO_3)_2{\cdot}6H_2O$ was dissolved in deionized water, and appropriated amounts of $Eu(NO_3)_3$ solution were added to the above

* Corresponding author at: Institute of Condensed State Physics, Jilin Normal University, Siping 136000, PR China. Tel.: +86 434 3294566; fax: +86 434 3294566.
E-mail address: jhyang1@jlnu.edu.cn (J. Yang).

0925-8388/$ – see front matter © 2011 Elsevier B.V. All rights reserved.
doi:10.1016/j.jallcom.2011.08.021

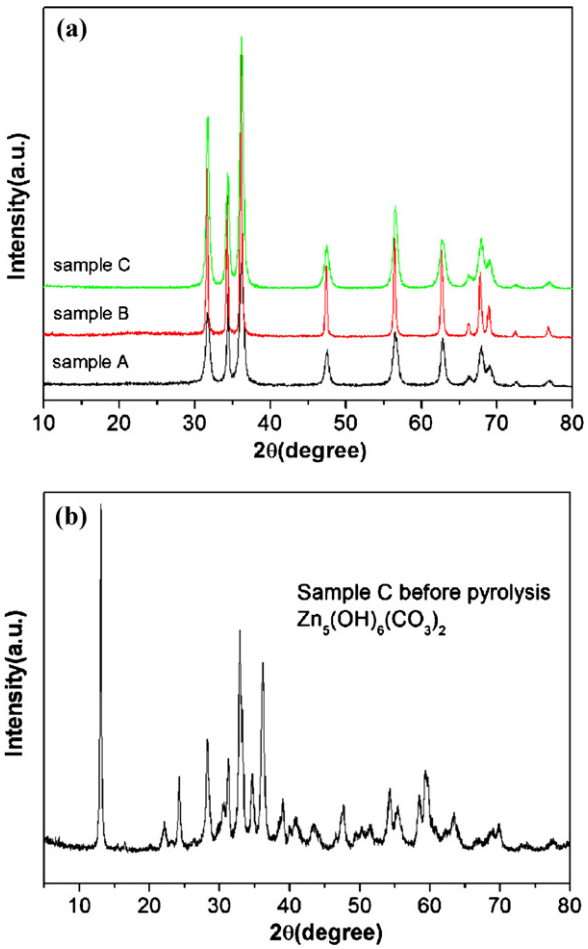

Fig. 1. XRD of ZnO:1%Eu nanomaterials with different mineralizing agents: (a) samples A, B and C and (b) precursor $Zn_5(OH)_6(CO_3)_2$ of sample C before annealing.

solution, then the mineralizing agents (NaOH, HMT and $(NH_2)_2CO$) were added to the above solution. Finally, the mixed solution was transferred into a 60 mL Teflon-lined stainless steel autoclave, which was heated at 155 °C for 24 h. After growth, the system was allowed to cool down to room temperature and the product was collected, washed with deionized water and ethanol for three times, separated by a centrifuge, and then dried in an oven at 60 °C for 1 h under air atmosphere to get white powder. The final product was annealed at 400 °C for 2 h in Ar gas atmosphere when $(NH_2)_2CO$ used as the mineralizing agent.

X-ray diffraction (XRD) (MAC Science, MXP18, Japan), X-ray photoelectron spectroscopy (XPS) (VG ESCALAB Mark II), scanning electron microscopy (SEM) (Hitachi, S-570), transmission electron microscope (TEM) (JEM-2100HR, Japan), photoluminescence spectroscopy (PL) (He–Cd Laser, 325 nm) and Raman (Invia-UV, UK) were used to characterize the crystal structures, morphologies and photoluminescence properties of the Eu-doped ZnO nanomaterials.

3. Results and discussion

Fig. 1 shows the XRD patterns of the as-prepared ZnO:1%Eu samples. The specific synthesis conditions of the samples can be seen in Table 1. Compared with the XRD standard pattern of ZnO [28], the diffraction peaks of all the samples in Fig. 1(a) can be indexed to the hexagonal wurtzite structure of ZnO, and no other peaks are detected from europium oxide or other impurities. Moreover, the sharp diffraction peaks of all the Eu-doped ZnO nanomaterials indicate that the samples prepared with the present method are highly crystallized. To clearly understand the growth process with adding different mineralizing agents, we would like to point out that the XRD results testify the ZnO:1%Eu samples can be synthesized by only one step with using NaOH and HMT as the mineralizing agents. While, as shown in Fig. 1(b), we can see that the initial product with adding $(NH_2)_2CO$ is not ZnO but the hydroxide zinc carbonate ($Zn_5(OH)_6(CO_3)_2$), which is easily pyrolyzed into ZnO by further annealing. Thus, the synthesis process of Eu-doped ZnO nanomaterials with mineralizing agent of $(NH_2)_2CO$ consists of two steps, i.e. hydrothermal reaction and annealing process. The Zn^{2+} ions first react with the OH^- and CO_3^{2-} originated from $(NH_2)_2CO$ to form an insoluble precursor at the bottom of the autoclave, and then decompose into wurtzite ZnO after further annealing at 400 °C.

Table 1
Synthesis conditions of the samples.

Sample	Mineralizing agent	Annealing temperature	Doping concentrations (molar ratio)
A	NaOH	–	1%
B	$C_6H_{12}N_4$(HMT)	–	1%
C	$(NH_3)_2CO$	400 °C	1%

X-ray photoelectron spectroscopy (XPS) and energy dispersive spectroscopy (EDS) are used to analyze the compositions of the ZnO:1%Eu samples. Fig. 2 shows the XPS spectra of ZnO:1%Eu samples. The binding energies (BE) have been calibrated by taking the carbon C1s peak (285.2 eV) as reference. As shown in the wide scan XPS spectra (Fig. 2(a)), the Zn2p3/2, Zn2p1/2, O1s, C1s and Eu3d have been detected, which indicates the elements of Zn, Eu, O and C exist in the as-prepared ZnO:1%Eu samples. The double peaks at 1044 eV and 1021 eV in Fig. 2(b) are corresponding to the core levels of Zn2p1/2 and Zn2p3/2 of ZnO, respectively. The fitting of O1s region with two Gauss functions indicates that at least two kinds of oxygen species are present in the near surface domain of three ZnO:1%Eu samples (Fig. 2(c)). The peak at ~530 eV can be ascribed to the crystal lattice oxygen of doped ZnO nanocrystals, while the peak at ~531.7 eV originates from the chemisorbed oxygen on the nanocrystal surfaces. The concentration of the elements present in the sample could be estimated using the formula $Cx\% = (In/Sn)/\sum In/Sn$, where x is the element and Sn is the sensitivity factor [29]. The O contents are about 63.73%, 81.19% and 59.23% in molarities, from which we can deduce that the concentrations of O-defects are 36.27%, 18.81% and 40.77% in molarities for samples A, B and C, respectively. Concerning the europium, four peaks of Eu3d are usually presented in the range of 1123–1167 eV. From Fig. 2(d), two peaks located at 1164.6 eV and 1134.7 eV can be assigned to the Eu3d3/2 and Eu3d5/2 core levels respectively, which indicates that the Eu ion has $a+3$ valence in Eu-doped ZnO sample [30]. In comparison with the standard binding energy of Eu3d5/2 (1135.6 eV), a blueshift of 0.9 eV in binding energy is observed for the sample C, meaning that the Eu–O distance in doped ZnO nanocrystals is quite different from that in pure Eu_2O_3 oxide [31,32]. Besides these lines, another two peaks are present at characteristic satellite structure, which are mainly attributed to final state effects and/or charge transfer coexcitations of light rare earth compounds. The energy separation of 9.8 eV between each satellite and the main spin orbit split component (marked with arrows shown in Fig. 2(d)) is in agreement with the previous report about Eu(III) oxides [33–35]. In addition, the XPS data shows the 0.86% Eu in molarity is detected in the ZnO:1%Eu sample. Meanwhile, the 0.81% Eu in molarity is also found in the same sample from the EDS spectrum (Fig. 3), which has a good agreement with XPS result.

Fig. 4 shows the morphologies of ZnO:1%Eu samples with different mineralizing agents. As expected, the morphologies of the samples grown with various mineralizing agents are significantly different. Sample A is composed of nanorods with diameter range of 12–20 nm, which can be clearly seen from the TEM image in Fig. 4(a). As shown in Fig. 4(b), the ZnO nanoneedle-based microflowers (sample B) are obtained when the mineralizing agent is fixed with HMT. The length of nanoneedles is 2–3 μm and the tip diameter is about 100 nm. Furthermore, TEM image indicates the

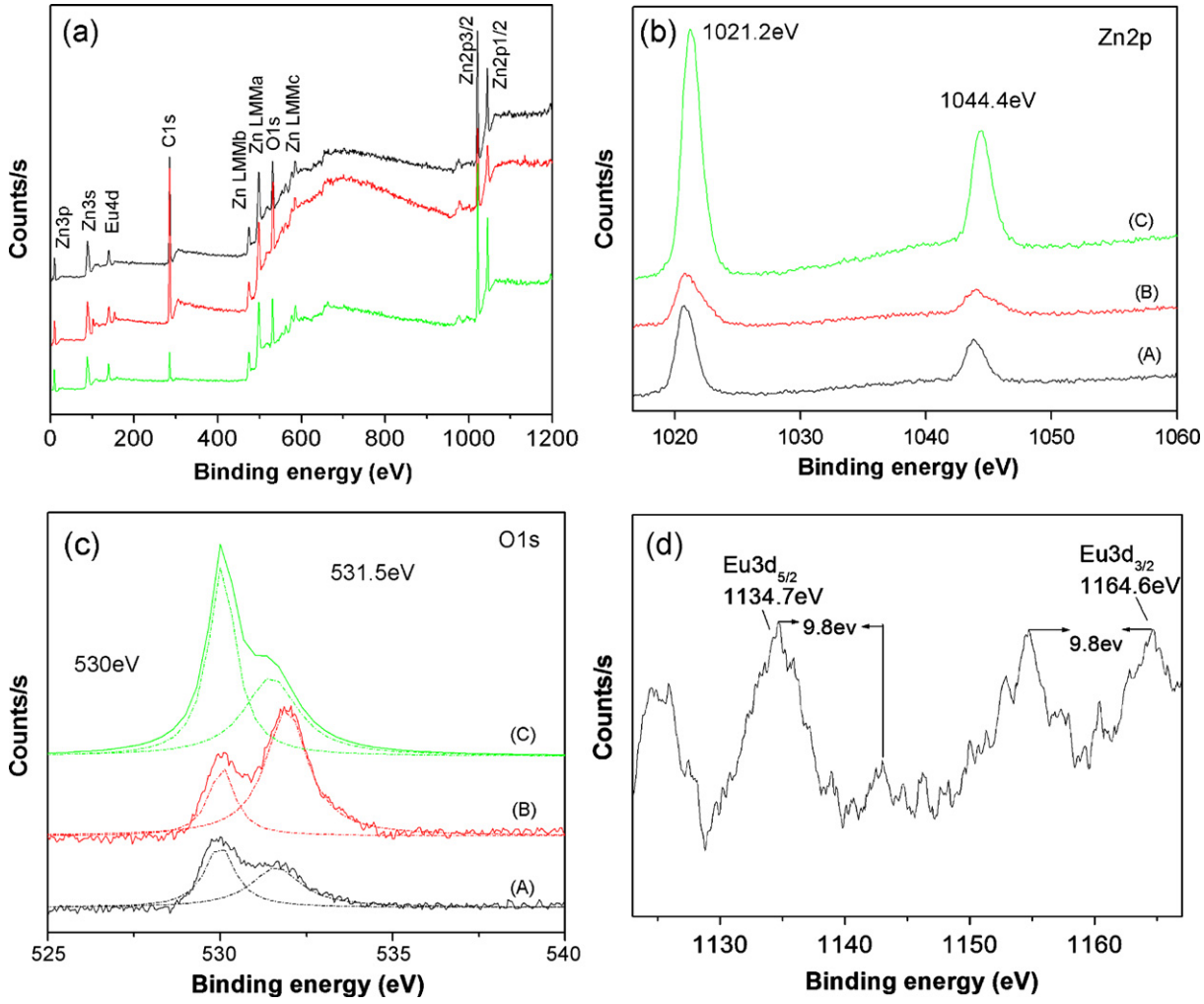

Fig. 2. XPS spectra of ZnO:1%Eu showing the individual (a) wide scan XPS spectra, (b) Zn2p, (c) O1s of three sample and (d) Eu3d peaks of sample C.

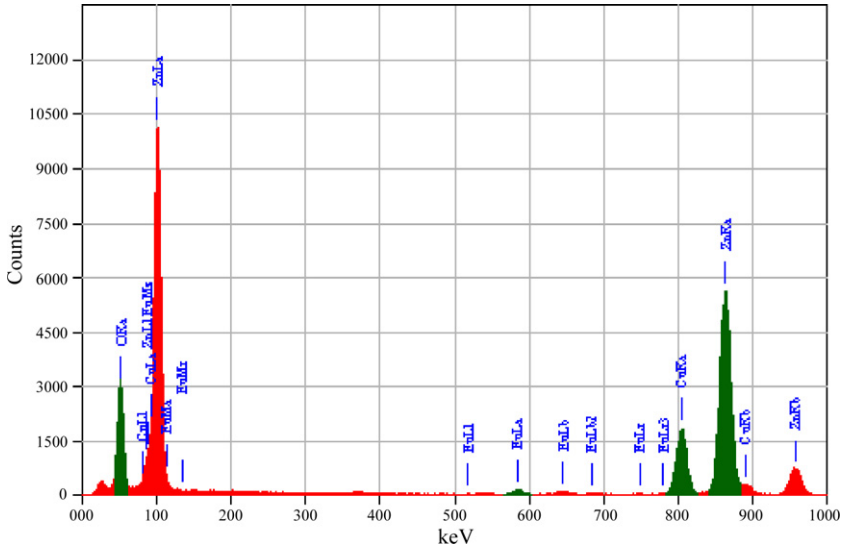

Fig. 3. EDS image of sample C.

morphology of sample C is the nanosheets with irregular porous microstructure (Fig. 4(c)). From the inset of Fig. 4(c), HRTEM image shows the clear lattice fringes with spacing of 0.267 nm between adjacent lattice planes correspond to the d-spacing of (0 0 0 2) plane of the Eu-doped ZnO sample, which is different from the undoped one (0.261 nm). It indicates that Eu^{3+} ions are successfully doped into the crystal lattice of ZnO matrix without forming europium oxides or any other impurities at the surface of ZnO.

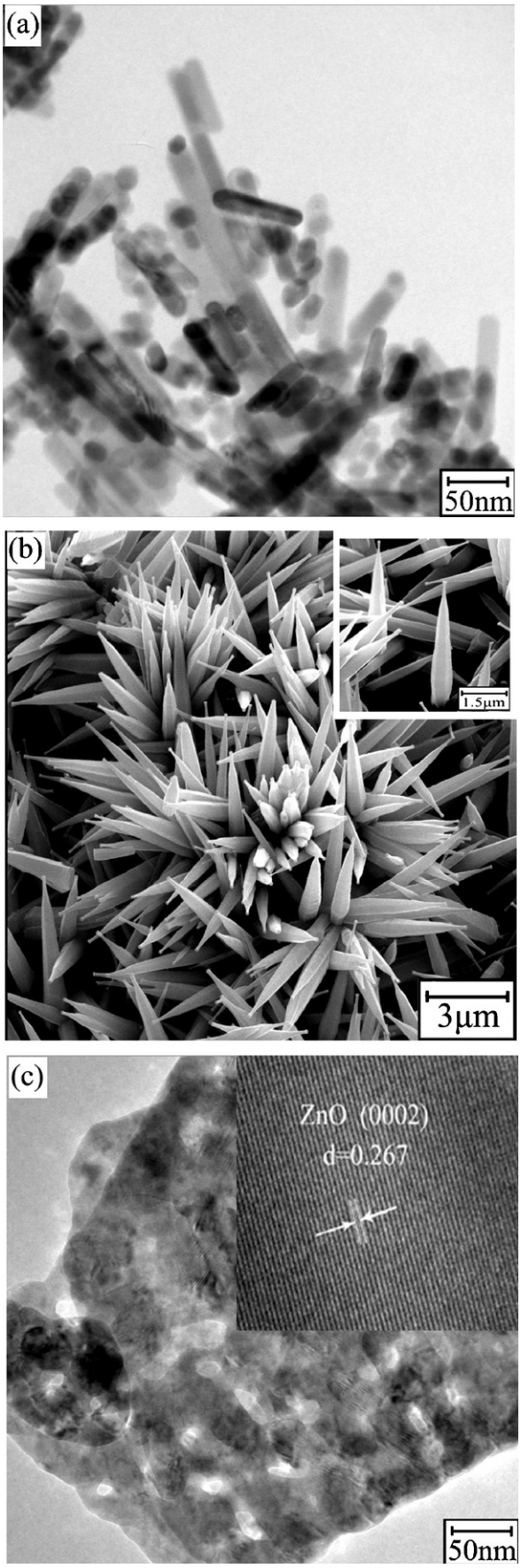

Fig. 4. Morphologies of ZnO:1%Eu nanomaterials with different mineralizing agents: (a) TEM image of sample A, (b) SEM image of sample B and (c) TEM image of sample C.

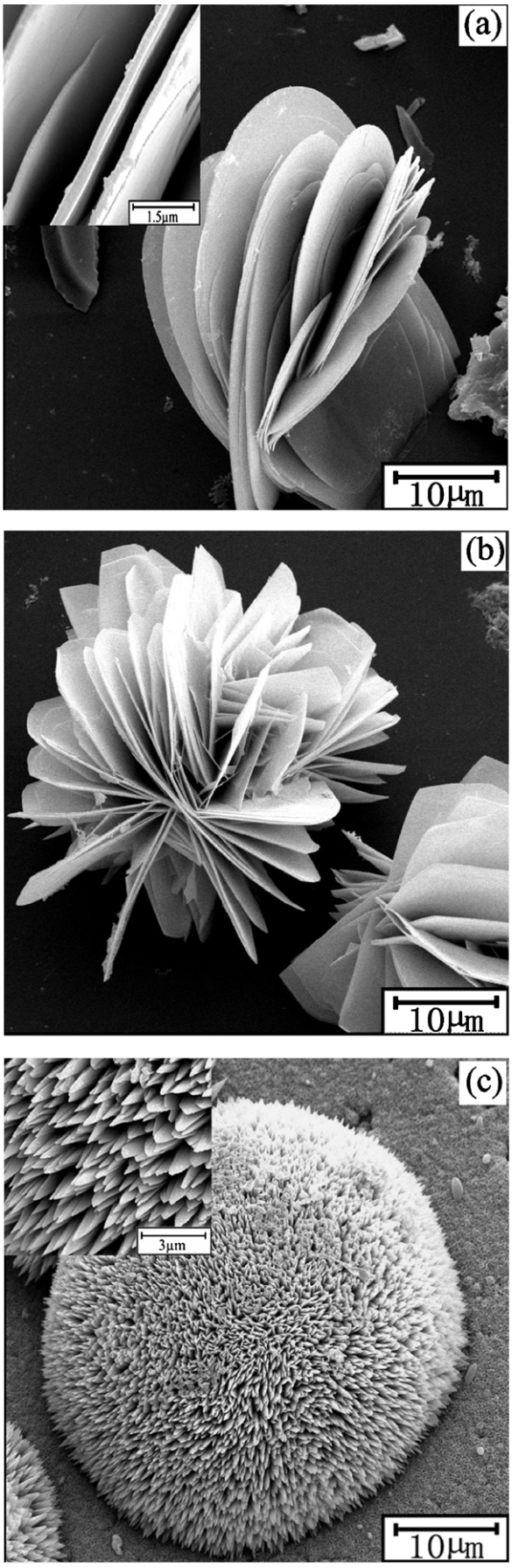

Fig. 5. SEM images of precursor (sample C) synthesized under different reaction time in the hydrothermal process: (a) 3 h, (b) 7 h and (c) 24 h.

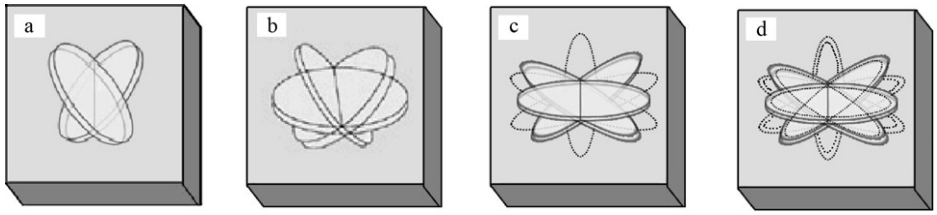

Fig. 6. A schematic representation for the formation and evolution of sample C by the first-step hydrothermal process: (a) ZnO nanosheets connect with each other to form a close stacking layer, (b) cactus-like microspheres assembled with single-crystal nanosheets and (c–d) etched process.

The morphologies of ZnO nanomaterials mainly depend on their growth conditions and mechanisms [36]. In our experiment, it is found that the obtained ZnO nanomaterials with different morphologies should be related to the release rate of OH^- in the solution due to the variation of mineralizing agents. The different release rate of OH^- in the reaction process could change the pH values in the resultant solution, which will decide the growth environment under the condition of neutrality or alkalescency. Thus, the crystal growth rate and orientation would be strongly influenced, which finally results in the difference of crystal morphology and body size for the as-grown ZnO nanomaterials.

In addition, optical properties of ZnO nanostructures are highly related to their morphologies [37]. The nanosheets with unique nanostructure may exhibit novel optical properties which is distinct from that of ZnO nanorods and nanoneedles. Therefore, the growth mechanism of nanosheets is worth for the further study. For the nanosheets, the $(NH_2)_2CO$ is used as the mineralizing agent in the experiment. As we know $(NH_2)_2CO$ as a homogeneous mineralizing agent has been widely exploited in synthesizing metal oxide nanostructures, and the morphologies and structures of nanomaterials could be controlled by adjusting specimen concentration, reaction time, and temperature [38,39]. In our case, we find that the reaction time plays an important role in controlling the microstructure of the obtained samples. The SEM images of the as-prepared precursors under different reaction time in the hydrothermal process are given in Fig. 5. As reaction time is 3 h, only partial and loosely nanosheets aggregate together to build small flower-like ZnO precursors, which can be seen in Fig. 5(a). It could be regarded as the early growth stage. With further increasing the reaction time to 7 h, the small flowers start to grow into larger cluster-like microspheres with more compact nanosheets (Fig. 5(b)). Furthermore, when the reaction time increases to 24 h, the cactus-like microspheres assembled with single-crystal nanosheets are obtained (Fig. 5(c)). According to the above growth variation with different reaction time, the formation mechanism of these nanostructures can be explained as follows in the schematic diagram (Fig. 6). The precursor crystallizes in a layered behavior in the (1 0 0) plane, in which the $[ZnO_6]$ octahedra and $[ZnO_4]$ tetrahedra connect with each other to form a close stacking layer, and the neighboring zinc oxide layers are combined by weak CO_3^{2-} and OH^- anions [40,41]. Hence, the nucleation and growth of the nanosheets are more likely to happen at the edge of each nanosheet, and the nanosheets are aligned with one another, which would lead to the cactus-like microspheres assembled with single-crystal nanosheets. Furthermore, the end of petals converts to point and the width of sheets becomes narrow with the reaction time increasing, which can be clearly seen in the inset. A possible explanation of this phenomenon is that the fringes of sheets would be etched due to the further increase of the pH value in the solution with prolonging the reaction time.

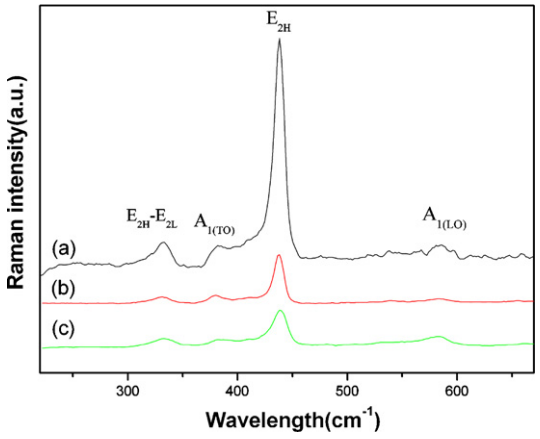

Fig. 7. Raman spectra of ZnO:1%Eu samples with different mineralizing agents: (a) sample A, (b) sample B and (c) sample C.

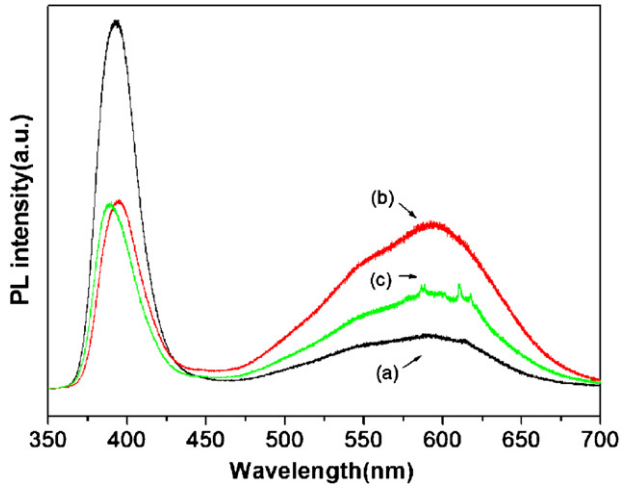

Fig. 8. Room temperature PL spectra of ZnO:1%Eu samples with different mineralizing agents: (a) sample A, (b) sample B and (c) sample C.

Fig. 7 shows the Raman spectra of ZnO:1%Eu samples with different mineralizing agents, which is excited by 514 nm line from an argon laser. In Fig. 7, the peaks located at 332, 382, 438, and 584 cm^{-1} can be observed. On the basis of the reported zone-center optical phonon frequencies in ZnO, the peaks located at 332 and 382 cm^{-1} can be assigned to E_{2H}–E_{2L} and $A_{1(TO)}$ Raman mode, respectively [42,43]. The sharp peak located at 438 cm^{-1} is attributed to the ZnO nonpolar optical phonons of E_{2H} mode, which is one of the characteristic peaks of wurtzite ZnO [44,30]. The Raman peak located at about 584 cm^{-1} corresponds to $A_{1(LO)}$ phonon, which is attributed the defects of O-vacancy, Zn-interstitial, or these complexes in the samples [45]. Comparing the three Raman spectra, it can be seen that the values of the full width at half maximum (FWHM) for the E_{2H} peak are different. To ascertain by computation, the FWHM values of E_{2H} peak for samples A, B, C are estimated to be about 9 cm^{-1}, 11 cm^{-1} and 15 cm^{-1}, respectively. The value of sample A is minimum, which indicates that the sample A has the best crystalline quality among the three samples.

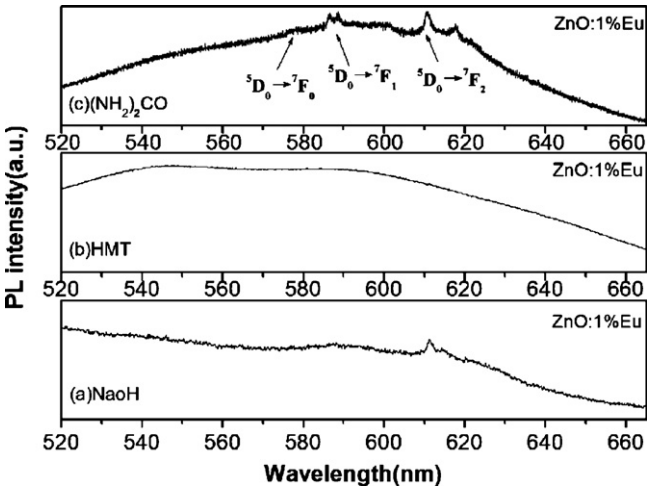

Fig. 9. Zoom to area of the defect emission of PL spectra in Fig. 5: (a) sample A, (b) sample B and (c) sample C.

Fig. 8 shows the photoluminescence spectra of ZnO:1%Eu samples with different mineralizing agents measured at room temperature. Samples are excited by a He–Cd laser at a wavelength of 325 nm. As seen in Fig. 8, all the spectra exhibit an ultraviolet (UV) emission and a defect emission. The UV emission centered at about 386 nm is originated from the recombination of the free excitons in ZnO [46–48]. The defect emission ranging from 440 nm to 700 nm is associated with deep level emission (DLE) in ZnO [4,49], which is related to the intrinsic defects such as O-vacancy (V_O) [50–52], Zn-vacancy (V_{Zn}) [53–55], O-interstitial (O_i) [56], Zn-interstitial (Zn_i) [57,58], and extrinsic impurities [59]. According to the XPS results, the Eu ions exist in the ZnO lattices with $a+3$ valence. In normal case, Eu ions are apt to take the places of Zn ion sites, thus the local charge balance in ZnO will be broken. In order to maintain the balance, the concentration of the defects such as V_{Zn} and O_i should be changed for charge compensation, resulting in variation of the crystalline quality [60]. From Fig. 8, we also can find that the relative PL intensity ratio of ultraviolet emission (I_{UV}) to deep level emission (I_{DLE}) of the samples with different mineralizing agents is quite different. To ascertain by computation [61], the intensity ratio of I_{UV}/I_{DLE} of samples A, B, C is estimated to be about 6.7, 1.1 and 1.8, respectively. The intensity ratio of I_{UV}/I_{DLE} is related with the crystallization, so the sample A with mineralizing agent of NaOH should have much better crystallization according to the larger intensity ratio, which has a good agreement with above Raman results.

In order to investigate the deep level emission of Eu^{3+} ion in detail, three PL spectra have been magnified in the range of 520–660 nm, as shown in Fig. 9. In the spectrum, the peaks located at 580, 587 and 614 nm are observed, which can be attributed to the 4f–4f intrashell transitions of $^5D_0 \rightarrow {}^7F_0$, $^5D_0 \rightarrow {}^7F_1$ and $^5D_0 \rightarrow {}^7F_2$ of Eu^{3+} ions, respectively [62]. Comparing three spectra, it can be seen the intensity of the defect emissions of samples A, B and C are obviously different. Interestingly, the red emissions of Eu^{3+} ions are found in samples A and C but disappear in sample B. In ZnO, the energy level of defects related to green emission is 2.3–2.45 eV [63], which is close to the excited state energy of Eu^{3+}, thus nonradiative energy transfer from these defects to Eu^{3+} ions is favorable. Therefore, the defects related to green emission have a great possibility to act as the energy storage centers in the energy transfer process. Recently, this deep level emission band had been identified and at least two different defect origins (V_O and V_{Zn}) with different optical characteristics were claimed to contribute to this DLE band [58,64,65]. In our case, Eu elements are doped into the ZnO matrix, and the results from both XRD and XPS already proves that the Eu^{3+} ions take the place of Zn^{2+} ions. Thus, the possibility to form V_{Zn} will be lowered so that V_O may play the domain role to contribute the green emission in our samples. So we believe that there is a strong correlation between the O-vacancies concentration and the characteristics of the Eu^{3+}-related red emission. The more concentration of O-vacancies exists in the samples, the more red emissions will be stronger. The conclusion can be further proved by the XPS results. From the XPS results, we can see the concentrations of O-defects are 36.27%, 18.81% and 40.77% in molarities for samples A, B and C, respectively. The sample B does not have enough O-vacancies concentration, so the sharp red emission disappears. In addition, when the $(NH_2)_2CO$ as mineralizing agent is introduced into the hydrothermal process, the red emissions of Eu^{3+} is more obvious (sample C). Therefore, the red emissions might be attributed to coordination with some anions (CO_3^{2-} or OH^-). The CO_3^2 or OH^- anions at the nonpolar surface might bring more oxygen defect and stabilize their levels just below the conduction band of ZnO, which facilitate the ZnO–Eu^{3+} energy transfer. From these results, we can clearly see that more defect appear in the system, more efficient and fast energy transfer occurs, especially, the O-vacancies can assist energy transfer process from the ZnO host to the Eu dopants.

4. Conclusions

In this work, we have successfully prepared Eu-doped ZnO nanorods, nanoneedles and cactus-like microspheres based on nanosheets with different mineralizing agents by a simple hydrothermal method, and further discussed the morphologies and optical properties of the samples in detail. The different morphologies of nanomaterials with various mineralizing agents should be related to the release rate of OH^- in the solution. The sample grown with mineralizing agent NaOH has much better crystallization according to the Raman and PL results. Moreover, the as-prepared Eu-doped ZnO nanomaterials with various morphologies exhibit different optical properties. From the PL results, the red emissions of Eu^{3+} is more obvious when the mineralizing agent is fixed at $(NH_2)_2CO$. The intensity of red emission is found to be related with the intrinsic defect emission and the intrinsic defects can assist efficient energy transfer from the ZnO host to the Eu^{3+} ions. More efficient Eu^{3+} emission is expected by the rational control of the concentration and type of mineralizing agents. The above results not only provides a simple hydrothermal method to fabricate Eu-doped ZnO nanomaterials with various morphologies, but also proves the possibility of realizing efficient RE^{3+} 4f–4f emission in ZnO nanostructures which could be utilized in various optoelectric applications.

Acknowledgements

This work is supported by the National Natural Science Foundation of China (Grant No. 60778040), Program for the development of Science and Technology of Jilin province (Item No. 20090140 and 20100113), the Eleventh Five-Year Program for Science and Technology of Education Department of Jilin Province (Item No. 20090422 and 20090187), program for importing foreign technology and management talents into China (Item No. S20072200001), the Open Project Program for National Laboratory of Superhard Materials (No. 201004) and Program for the Development of Science and Technology of Jilin province (Item No. 20070707).

References

[1] Yun Geng Zhang, Guang Biao Zhang, Yuan Xu Wang, J. Appl. Phys. 109 (2011) 063510.

[2] J.H. Yang, J.H. Zheng, H.J. Zhai, X.M. Yang, L.L. Yang, Y. Liu, J.H. Lang, M. Gao, J. Alloys Compd. 489 (2010) 51.
[3] Yusuf Selim Ocak, Mustafa Kulakci, Rasit Turan, Tahsin Kilicoglu, Omer Gullu, J. Alloys Compd. 509 (2011) 6631.
[4] J.H. Yang, R. Wang, L.L. Yang, J.H. Lang, M.B. Wei, M. Gao, X.Y. Liu, J. Cao, X. Li, N.N. Yang, J. Alloys Compd. 509 (2011) 3606.
[5] Achamma George, S.K. Sharma, Santa Chawla, M.M. Malik, M.S. Qureshi, J. Alloys Compd. 509 (2011) 5942.
[6] M.G. Zhao, X.C. Wang, L.L. Ning, H. He, J.F. Jia, L.W. Zhang, X.J. Li, J. Alloys Compd. 507 (2010) 97.
[7] Jinghai Yang, Xue Li, Jihui Lang, Lili Yang, Maobin Wei, Ming Gao, Xiaoyan Liu, Hongju Zhai, Rui Wang, Yang Liu, Jian Cao, Mater. Sci. Semiconduct. Process., doi:10.1016/j.mssp.2011.04.002.
[8] D.D. Wang, G.Z. Xing, J.H. Yang, L.L. Yang, M. Gao, J. Cao, Y.J. Zhang, B. Yao, J. Alloys Compd. 504 (2010) 22.
[9] S.K. Lathika Devi, K. Sudarsana Kumar, A. Balakrishnan, Mater. Lett. 65 (2011) 35.
[10] Alessandri, M. Zucca, M. Ferroni, E. Bontempi, L.E. Depero, Cryst. Growth Des. 9 (2009) 1258.
[11] S.S. Shinde, K.Y. Rajpure, J. Alloys Compd. 509 (2011) 4603.
[12] Sheng-Rui Jian, J. Alloys Compd. 494 (2010) 214.
[13] Yinxiao Du, Fanguang Zeng, Mater. Lett. 65 (2011) 2238.
[14] T. Li, C.S. Ong, T.S. Herng, J.B. Yi, N.N. Bao, J.M. Xue, Y.P. Feng, J. Ding, Appl. Phys. Lett. 98 (2011) 152505.
[15] Y.J. Fang, J. Sha, Z.L. Wang, Y.T. Wan, W.W. Xia, Y.W. Wang, Appl. Phys. Lett. 98 (2011) 033103.
[16] L.Q. Zhang, Z.Z. Ye, B. Lu, J.G. Lu, Y.Z. Zhang, L.P. Zhu, J.Y. Huang, W.G. Zhang, J. Huang, J. Zhang, J. Jiang, K.W. Wu, Z. Xie, J. Alloys Compd. 509 (2011) 2149.
[17] A. Jagannatha Reddy, M.K. Kokila, H. Nagabhushana, R.P.S. Chakradhar, C. Shivakumara, J.L. Rao, B.M. Nagabhushana, J. Alloys Compd. 509 (2011) 5349.
[18] A. Azam, F. Ahmed, N. Arshi, M. Chaman, A.H. Naqvi, J. Alloys Compd. 496 (2010) 399.
[19] S.S. Alias, A.B. Ismail, A.A. Mohamad, J. Alloys Compd. 499 (2010) 231.
[20] W.E. Mahmoud, J. Cryst. Growth 312 (2010) 3075.
[21] P.M. Aneesh, M.K. Jayaraj, Bull. Mater. Sci. 33 (2010) 227.
[22] Badalawa, Wasanthamala Matsui, Hiroaki Osone, Takamasa Hasuike, Noriyuki Harima, Hiroshi Tabata, Hitoshi, J. Appl. Phys. 109 (2011) 053502.
[23] Yongsheng Tan, Zebo Fang, Wei Chen, Pimo He, J. Alloys Compd. 509 (2011) 6321.
[24] Dengsong Zhang, Tingting Yana, Liyi Shi, Hongrui Li, J.F. Chiang, J. Alloys Compd. 506 (2010) 446.
[25] Chockalingam Karunakaran, Paramasivan Gomathisankar, Govindasamy Manikandan, Mater. Chem. Phys. 123 (2010) 585.
[26] M.Y. Zhong, G. Shan, Y.J. Li, G.R. Wang, Y.C. Liu, Mater. Chem. Phys. 106 (2007) 305.
[27] Y.J. Sun, Y. Chen, L.J. Tian, Y. Yu, X.G. Kong, Q.H. Zeng, Y.L. Zhang, H. Zhang, J. Lumin. 128 (2008) 15.
[28] O. García Martínez, R.M. Rojas, E. Vila, J.L. Martín de Vidales, Solid State Ionics 63 (1993) 442.
[29] S. Akanksha, L. Mukta, S. Shashi, P.L. Niranjan, C.K. Malek, S. Kulkarni, Nanotechnology 19 (2008) 245613.
[30] T.C. Damen, S.P.S. Porto, B. Tell, Phys. Rev. 142 (1966) 570.
[31] L. Yang, Y. Li, Y. Xiao, C. Ye, L.D. Zhang, Chem. Lett. 6 (2005) 34.
[32] Y.P. Du, Y.W. Zhang, L.D. Sun, C.H. Yan, J. Phys. Chem. C 112 (2008) 12234.
[33] F. Mercier, C. Alliot, L. Bion, N. Thromat, P.J. Toulhoat, J. Electron. Spectrosc. Relat. Phenom. 150 (2006) 21.
[34] W.D. Schneider, C. Laubshat, I. Nowik, G. Kaindl, Phys. Rev. B: Condens. Matter Mater. Phys. 24 (1981) 5422.
[35] C. Laubshat, B. Perscheid, W.D. Schneider, Phys. Rev. B: Condens. Matter Mater. Phys. 28 (1983) 4342.
[36] W. Yu, C.X. Pan, Mater. Chem. Phys. 115 (2009) 74.
[37] I. Shalish, H. Temkin, V. Narayanamurti, Phys. Rev. B 69 (2005) 245401.
[38] C. Yan, D. Xue, J. Phys. Chem. B 110 (2006) 11076.
[39] E. Hosono, S. Fujihara, I. Honma, H. Zhou, Adv. Mater. 17 (2005) 2091.
[40] S. Ghose, Acta Crystallogr. 17 (1964) 1051.
[41] X.Y. Zeng, J.L. Yuan, L.D. Zhang, J. Phys. Chem. C 112 (2008) 3503.
[42] J.H. Lang, Q. Han, J.H. Yang, C.S. Li, X. Li, L.L. Yang, J. Appl. Phys. 107 (2010) 074302.
[43] L.L. Yang, J.H. Yang, D.D. Wang, Y.J. Zhang, Y.X. Wang, H.L. Liu, H.G. Fan, J.H. Lang, Physica E 40 (2008) 920.
[44] A. Kaschner, U. Haboeck, M. Strassburg, G. Kaczmarczyk, A. Hoffmann, C. Thomsen, A. Zeuner, H.R. Alves, D.M. Hofmann, B.K. Meyer, Appl. Phys. Lett. 80 (2002) 1909.
[45] X. Wang, Q. Li, Z. Liu, J. Zhang, Z. Liu, R. Wang, Appl. Phys. Lett. 84 (2004) 4941.
[46] D. Weissenberger, M. Dürrschnabel, D. Gerthsen, Appl. Phys. Lett. 91 (2007) 132110.
[47] W.I. Park, Y.H. Jun, S.W. Jung, Appl. Phys. Lett. 82 (2003) 964.
[48] P.L. Chen, X.Y. Ma, D.R. Yang, J. Alloys Compd. 431 (2007) 317.
[49] L. Kumari, W.Z. Li, Cryst. Res. Technol. 45 (2010) 311.
[50] P.H. Kasai, Phys. Rev. 130 (1963) 989.
[51] S. Yamauchi, Y. Goto, T. Hariu, J. Cryst. Growth 260 (2004) 1.
[52] D.D. Wang, J.H. Yang, L.L. Yang, Y.J. Zhang, J.H. Lang, M. Gao, Cryst. Res. Technol. 43 (2009) 1041.
[53] M. Liu, A.H. Kitai, P. Mascher, J. Lumin. 54 (1992) 35.
[54] E.G. Bylander, J. Appl. Phys. 49 (1978) 1188.
[55] X. Yang, G. Du, X. Wang, J. Wang, B. Liu, Y. Zhang, D. Liu, D. Liu, H.C. Ong, S. Yang, J. Cryst. Growth 252 (2003) 275.
[56] J. Zhong, A.H. Kitai, P. Mascher, W. Puff, J. Electrochem. Soc. 140 (1993) 3644.
[57] L.L. Yang, Q.X. Zhao, M. Willander, J.H. Yang, Ivanov, J. Appl. Phys. 105 (2009) 053503.
[58] Q.X. Zhao, P. Klason, M. Willander, Appl. Phys. Lett. 87 (2005) 211912.
[59] R. Dingle, Phys. Rev. Lett. 23 (1969) 579.
[60] S. Fujihara, A. Suzuki, T. Kimura, J. Appl. Phys. 94 (2003) 2411.
[61] J.H. Lang, J.H. Yang, C.S. Li, L.L. Yang, Q. Han, Y.J. Zhang, D.D. Wang, M. Gao, X.Y. Liu, Cryst. Res. Technol. 43 (12) (2008) 1314.
[62] S.S. Ashtaputre, A. Nojima, S.K. Marathe, D. Matsumura, T. Ohta, R. Tiwari, G.K. Dey, S.K. Kulkarni1, J. Phys. D: Appl. Phys. 41 (2008) 015301.
[63] K. Vanheusden, W.L. Warren, C.H. Seager, D.R. Tallant, J.A. Voigt, B.E. Gnade, J. Appl. Phys. 79 (1996) 7983.
[64] T. Moe Børseth, B.G. Svensson, A.Yu. Kuznetsov, P. Klason, Q.X. Zhao, M. Willander, Appl. Phys. Lett. 89 (2006) 262112.
[65] P. Klason, T.M. Børseth, Q.X. Zhao, B.G. Svensson, A.Y. Kuznetsov, M. Willander, Solid State Commun. 145 (2008) 321.